The Astrophysical Journal Letters, 937:L23 (9pp), 2022 October 1 https://doi.org/10.3847/2041-8213/ac905a

Sodium Distribution on the Moon

S. Narendranath[1], Netra S. Pillai[1], Srikar P. Tadepalli[1,2], Menelaos Sarantos[3], K. Vadodariya[1], A. Sarwade[1], Radhakrishna V[1], and A. Tyagi[1]
[1] U R Rao Satellite Centre Indian Space Research Organisation Bengaluru, India
[2] IIT Banaras Hindu University, India
[3] Heliophysics Science Division, NASA Goddard Space Flight Center Greenbelt, MD, USA
Received 2022 August 3; revised 2022 August 30; accepted 2022 September 8; published 2022 September 26

Abstract

The Moon is significantly depleted in volatile elements when compared to Earth, an observation that has resulted in various formation scenarios leading to the loss of volatiles. Sodium is a moderately volatile element that is a lithophile, which can be utilized as a tracer of the volatile history in planetary bodies. It is also well observed in the exosphere of several bodies in our solar system and exoplanetary systems. But lunar surface sodium abundances have so far been measured only in samples brought back to Earth. We report on results from the first effort to provide a global-scale measurement of sodium on the lunar surface using X-ray fluorescent spectra from Chandrayaan-2. A global average of 1.33 ± 0.03 wt% derived here is higher than previously known. Trends in the sodium abundance indicate a long-lived adsorbate component that could explain the higher abundances reported here, which would act as a reservoir that sustains the lunar sodium exosphere.

Unified Astronomy Thesaurus concepts: Surface composition (2115); Lunar surface (974); Exosphere (499); Spectroscopy (1558)

1. Introduction

Sodium (Na) is a moderately volatile element with a 50% condensation temperature of about 1000 K (Lodders 2003; Wood et al. 2019) that is highly depleted in returned lunar samples in comparison to terrestrial basalts (Ringwood & Kesson 1977). It is primarily hosted in the lunar minerals plagioclase feldspar and pyroxene. Plagioclase feldspars occur as solid solutions between albite ($NaAlSi_3O_8$) and anorthite ($CaAl_2Si_2O_8$) and when compared to terrestrial plagioclases, lunar plagioclases are more anorthitic, indicative of alkali depletion on the Moon. The reported Na abundances in the returned soil (bulk composition) samples from Apollo, Luna, and Chang'e-5, however, span a range from 0.3 to 0.72 wt% and are higher in basaltic samples. The upper limit on Na abundances in meteoritic samples is also about 0.7 wt%. Since these measurements are highly localized and limited in spatial extent, we do not have a complete understanding of how sodium and such minor elements vary across the Moon. Though Na is a minor component of the lunar regolith, it is well observed in the lunar exosphere which extends beyond one lunar radius, with a tail (Smith et al. 1999; Baumgardner et al. 2021) that extends much further. Ground (Potter & Morgan 1988; Killen et al. 2019, 2021) and in-orbit (Szalay et al. 2016; Colaprete et al. 2016) measurements of the sodium exosphere have shown its temporal and spatial variability. While much of the temporal variability could be attributed to the surface release of Na by meteoritic impacts and geotail transit times, the spatial variability is harder to explain. Potassium (K) in the lunar exosphere (measured at low altitudes with the Lunar Atmosphere and Dust environment Explorer, LADEE) is shown to be correlated with surface K (Colaprete et al. 2016) with significant enhancements above the Procellarum KREEP terrane. Surface-exosphere correlations are also observed for Mercury (Merkel et al. 2018; Suzuki et al. 2021) specific to the element of interest, pointing to the fact that there are multiple parameters that determine the rate of retention and release mechanisms that sustain the surface boundary exosphere. A key missing element in the case of the Moon has been the complete lack of knowledge on the surface distribution of sodium, which is the primary reservoir for the exosphere.

Direct spectroscopic signatures of sodium exist only in X-rays and gamma-rays among remote sensing techniques. Detection of the sodium Kα line in the lunar X-ray spectrum was reported by Narendranath et al. (2011), Weider et al. (2012), and Athiray et al. (2014) using data from the Chandrayaan-1 X-ray Spectrometer (C1XS) (Grande et al. 2009) but was limited to four observations on the nearside of the Moon. Weider et al. (2012) suggested the detection to be a possible scattered component from solar X-rays while Athiray et al. (2014) concluded the presence of higher sodium abundances at specific regions of the Moon. Yamashita & Prettyman (2021) reported the detection of gamma-ray lines (not abundances) of sodium at 440 and 472 keV in the globally averaged lunar gamma-ray spectrum obtained with Kaguya-GRS with overlapping lines from Zn and B.

The Chandrayaan-2 Large Area Soft X-ray Spectrometer (CLASS) (Vatedka et al. 2020) is an enhanced version of C1XS with four times the collecting area, enabling measurements of fainter signals at a higher spatial resolution of 12.5 km. The X-ray Solar Monitor (XSM) (Mithun et al. 2020) on Chandrayaan-2 simultaneously measures the soft X-ray spectrum of the solar flare. We report X-ray fluorescence (XRF) detected from the Na-Kα line in lunar X-ray spectra collected over a period of two years from 2019 September to 2021 October. We used XRF emission models based on Shiraiwa & Fujino (1966) and a scattered component calculated from the measured solar spectrum to derive the elemental abundances. Monte Carlo simulations were performed to model

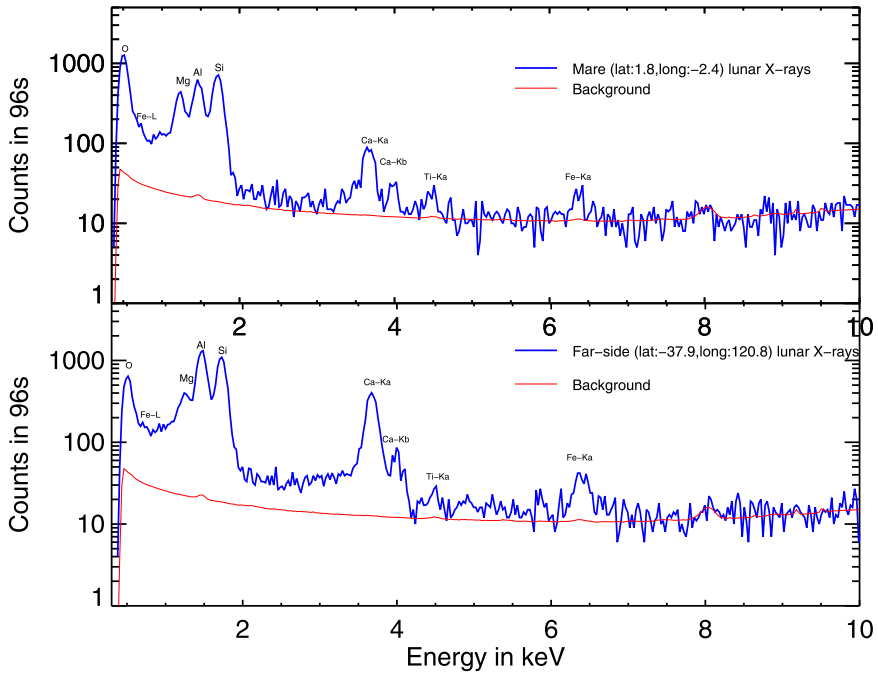

Figure 1. Lunar X-ray spectra from a mare region (above) and a farside non-mare region (below) are shown with the nominal background on the nightside (summed over a month). Along with the major elements from O to Fe, Ti, a minor element in these regions, is also detected.

the observed trend in sodium distribution that suggests two components in the XRF signal, one arising from the lunar regolith and another from a surface adsorbate layer. This is the first widespread, spectroscopic X-ray detection and abundance mapping of sodium on the lunar surface. Pieces of evidence for a volatile component of sodium are presented that are fundamental to our understanding of the Na surface boundary exosphere.

2. Data and Methods

2.1. Instrument

CLASS is an X-ray spectrometer with an operating energy range of ∼0.5–20 keV with a geometric collecting area of 64 cm^2, the largest flown to the Moon. There are 16 swept charge devices (SCDs) (Lowe et al. 2001), a non-imaging variant of X-ray CCDs, also flown on SMART1-DCIXS (Grande et al. 2007), Chandryaan-1 C1XS (Grande et al. 2009), and the Hard X-ray Modulation Telescope (HXMT) (Zhang et al. 2020). The SCD characteristics are well studied in the past leading to a good understanding of the most crucial parameter in X-ray spectroscopy: the spectral redistribution function (SRF). The SRF defines the probability of how a photon of a certain energy would be redistributed in the X-ray detector as the charge is detected and read-out. A detailed model of how the SRF is constructed and implemented as a response matrix (RMF) for analysis of CLASS X-ray spectra is given by Athiray et al. (2015). The detection efficiency of the SCD was measured at the BESSY II PTB Synchrotron facility (Smith et al. 2014) and is implemented as an ancillary response file (ARF). Copper collimators coated with gold define the $\pm 7\overset{\circ}{.}2$ field of view of the SCDs. The effective blocking fraction of the slat collimators was measured to be 15.5% on the ground. Two aluminum sheets of 2000 Å thickness each, supported on polyamide are used to block visible light from the Moon. The transmission loss through these filters are also part of the ARF. The instrument response thus takes into account all elements of the instrument. Onboard ^{55}Fe radioactive sources were used to verify the instrument response model. The calibration and in-flight performance is described in detail by Pillai et al. (2021).

2.2. Detection Limits

The strength of the XRF signal from the Moon is primarily dependent on the solar X-ray flux and spectral shape. While major elements (>1 wt%) are readily detected at 8 s cadence during strong solar flares (∼C5 flares and above), minor elements (<1 wt%) such as Na, Cr, and Mn are detected at coarser time intervals. Ti, an element that has a large range in abundances across the Moon, can be used as a test case to quantify how low an abundance can be detected by CLASS. It should be noted that detection also depends on the flux of solar X-rays that are incident with an energy greater than the binding energy of the K shell of the element (which is the strongest and is typically observed). Figure 1 shows spectra with Ti XRF lines detected from two different regions (nearside mare and farside non-mare) at nearly the same solar flare strength level. The Ti abundances from the Lunar Prospector (LP) Gamma Ray Spectrometer (GRS) at these regions (∼0.7 wt% in the mare and ∼0.2 wt% in the non-mare farside region) show that CLASS detects XRF signal from minor elements. As seen in Figure 1, the background in CLASS arises from the deposition of energy by particles an order of magnitude lesser than the XRF signal. We use a background from the nightside of the orbit either before or after the observation of interest. Figure 2 shows a detection of Cr and Mn XRF lines along with other elements from a region in the Mare Tranquillitatis, which are also minor elements on the Moon. We will be able to get a better constraint on the detection thresholds for the higher atomic number minor elements with solar activity picking up in recent months.

Owing to the low (∼1.07 keV for K shell) binding energy of the K shell electron of sodium, weaker solar flares (without

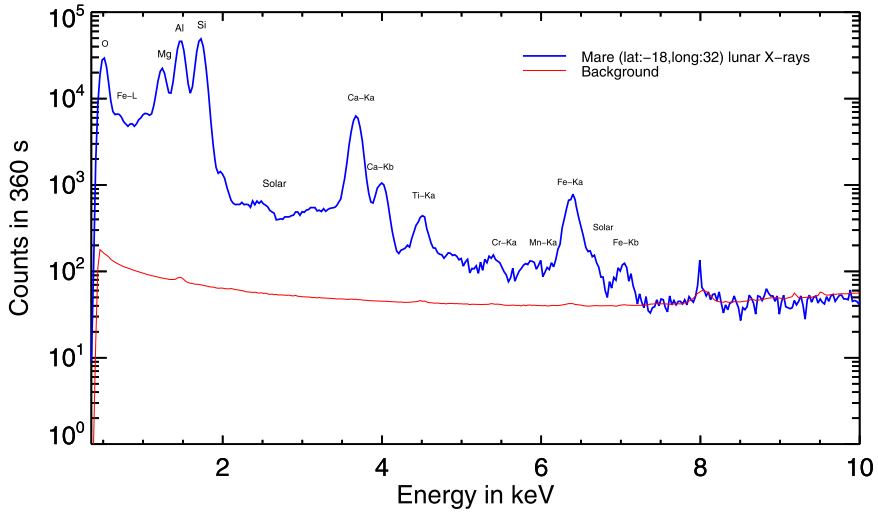

Figure 2. Lunar X-ray spectrum from a region in Mare Tranquillitatis showing the detection of minor elements Cr and Mn. The nominal background spectrum from the nightside (summed over a month) is also plotted.

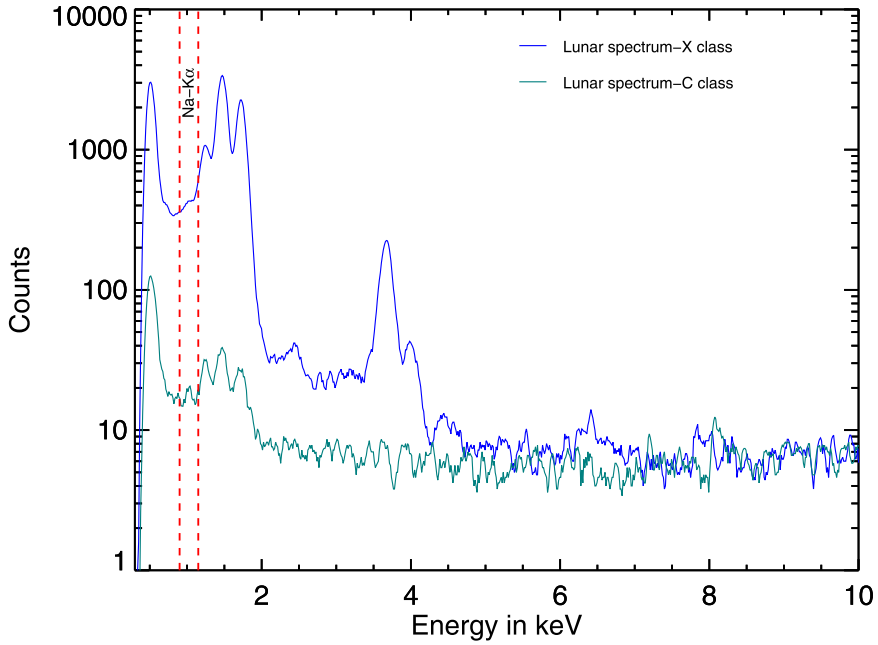

Figure 3. Lunar X-ray spectrum triggered by solar flares of two different classes showing the better detection of the sodium line in the weaker flare (C class). The slope of the scattered continuum is steep (more low-energy photons compared to high-energy) and high at low energies for stronger flares because the Na-Kα line to continuum ratio is very low.

detectable hard X-rays) can also trigger Na-Kα emission. Unlike other major elements, a visual inspection of the spectra does not always readily reveal such lines due to the high continuum at low energies. Figure 3 shows two cases of a lunar XRF spectrum with solar flares of different strengths, where the Na-Kα line is visible in the case of the C-class flare and not in the X-class flare. A confirmed detection therefore requires deconvolving the incident spectra using the instrument response with a model component including solar scattering.

2.3. Data Analysis

CLASS lunar X-ray spectra obtained during the period from 2019 September 14 to 2021 October 31st were used to identify time intervals when there was an XRF signal from Mg, Al, and Si. We then generated spectra of 96 s in each of these time intervals to look for the Na-Kα XRF line. A scattered solar spectral model was calculated using the measured solar spectrum from XSM. At times when XSM spectra were not available (as Sun was not in its field of view), we used the solar plasma temperature estimated from GOES-16 XRS. The abundances derived in either case are consistent for elements up to Ca, beyond which the GOES-16 XRS broadband flux does not adequately represent the solar spectrum. Figure 4 shows the wt% derived for Na and Mg, using XSM and GOES-16 XRS for a solar flare on 2021 August 27 as an example. Gaussian functions (for the observed XRF lines) and a scattered continuum were simultaneously fitted to each of the background-subtracted spectra. The background in the instrument arises from ambient particles and varies during geotail

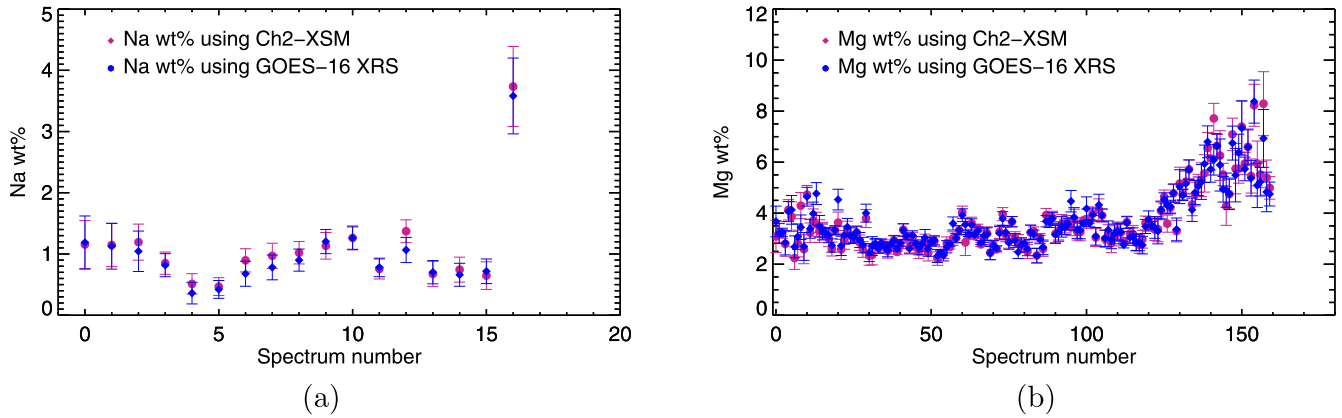

Figure 4. (a) Na wt% and (b) Mg wt% derived from CLASS data using Chandrayaan-2 XSM and GOES-16 XRS, which show consistency in the derived values.

passages. We have chosen the nightside background an orbit before or after from the observations. In cases where the geotail passage resulted in strong transient backgrounds, we used a nightside background averaged over several orbits. In order to estimate the abundances, we fit the selected spectra (with Na-Kα detections) with an XRF model expected for the incident solar spectrum for the geometry of observation. We begin with a matrix of elemental weight percentages and, in an iterative manner, derive the best-fit abundances using chisquare minimization. The scattered solar spectrum is also a component of the model. For those elements not observed in the lunar spectrum, we use the abundances from the LP-GRS data from the Planetary Data System (PDS) Geosciences Node (https://pds-geosciences.wustl.edu/lunar/lp-l-grs-5-elem-abundance-v1/lp_9001/) at the location. The method is described by Pillai et al. (2021) and references therein. A difference from the previous description is in the implementation of the algorithm to determine the abundances (Athiray et al. 2013a, 2013b). We incorporated the XRF model as a local model (via the python-based interface pyxspec) in the X-ray Spectral Analysis Package (XSPEC) (https://heasarc.gsfc.nasa.gov/xanadu/xspec/) that is widely used in X-ray astronomy. This enabled us to use the XSPEC fitting routines to arrive at the best-fit abundances. The local model as a zip file is available at https://pradan.issdc.gov.in/pradan/ch2/.

2.3.1. Uncertainties

The major sources of uncertainties in determining the abundances from CLASS are

1. The solar coronal abundances vary during a solar flare (Narendranath et al. 2020; Katsuda et al. 2020; Mondal et al. 2021). For the cases where GOES XRS 16 is used, this variation in the solar spectra (which will affect the strength of the scattered solar lines) is not considered. However as shown in Figure 5, for the strong flares used in this work, the XRF line intensities are approximately an order higher than the scattered solar lines.
2. For observations where Ca, Ti, and Fe are not detected by CLASS, we use values from LP-GRS for the corresponding pixel (an area-weighted average of overlapping pixels from both instruments) for the XRF model. The LP-GRS values are frozen during the fit and any associated uncertainty in these are not propagated. As the CLASS coverage of these elements will improve as solar activity picks up, we will be able to overcome this.

The model for the Na distribution presented here is largely based on the trends in distribution and hence associated errors in the absolute values, which do not affect the conclusions significantly.

3. Results

The Na-Kα XRF line at 1.04 keV is detected in lunar X-ray spectra with a 96 s integration time. As CLASS is a non-imaging instrument, the integration time translates to a ground trace of 150 km (along track) $\times$ 12.5 km(across track). Of the 1750 time intervals with XRF enhancement (3σ), we derive abundances from 1086 spectra. The sodium abundance map is overlaid on the LROC Wide Angle Camera (WAC) global albedo map in Figure 6. The northeastern high latitudes have a higher abundance of sodium. For a given track, there is a trend of increasing sodium toward the lunar poles. The abundance values also vary as a function of the local solar time (LST). These trends suggest an additional non-geochemical component to the observed sodium XRF intensity.

3.1. A Two-component Model for the Na Abundance

Apollo sample studies have shown that many of the mineral grains are encased in an amorphous layer of impact-generated vapors (Keller & McKay 1993), and that these coatings are enriched in volatile elements. Keller & McKay (1993) found an enhancement in S and Si but not in the alkali elements Na and K. They stated the possibility that the apparent lack of expected enhancement in the rims could be either a limitation of the analysis technique or, more interestingly, because it is the source of the neutral atoms in the exosphere (and is thus lost from the returned samples). If present globally, such a surface layer of alkali enrichment can be detected by XRF spectroscopy where the penetration depth is less than 2 μm for a 1 keV X-ray photon in a plagioclase regolith composition. An adsorbate layer, i.e., grain coatings made of sodium atoms previously released from the solid by energetic processes such as meteoroid impacts and sputtering, could also be consistent with the observed latitude dependence as adsorbates would accumulate at high latitudes due to their decreased outgassing rates there. The Na XRF line intensity emitted from a surface adsorbate layer versus that emitted from sodium placed in a compositional matrix will vary differently compared to the line flux from other elements. We simulated two scenarios of such a model with the Monte Carlo simulation toolkit Geant4 (Agostinelli et al. 2003) where the observed sodium XRF line

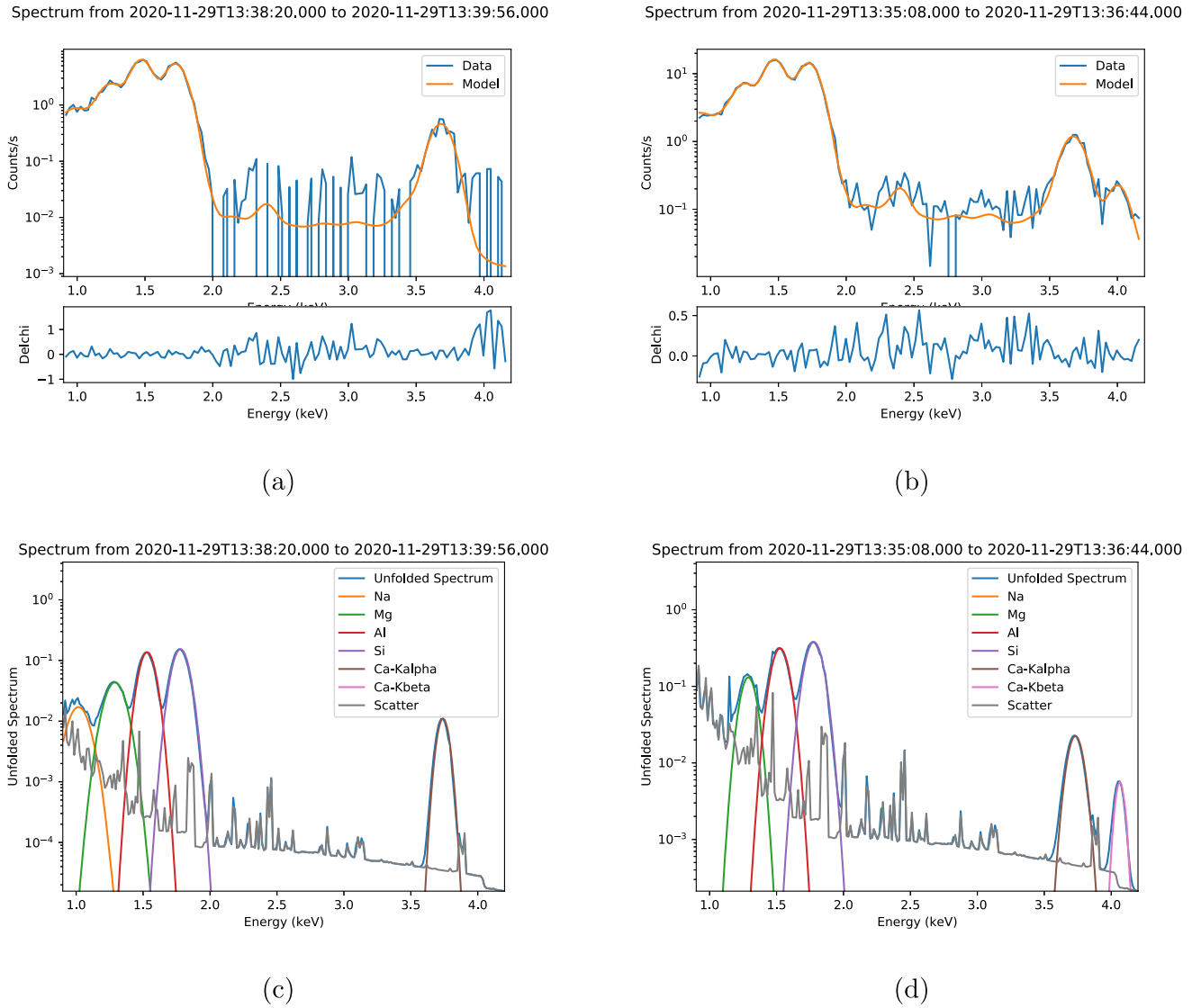

Figure 5. Spectral fits to lunar X-ray spectra showing two cases with and without sodium. Spectrum (a) shows the case when Na is detected and (b) where it is not. The deconvolved spectra are plotted in (c) and (d), showing the solar scattered component and XRF lines.

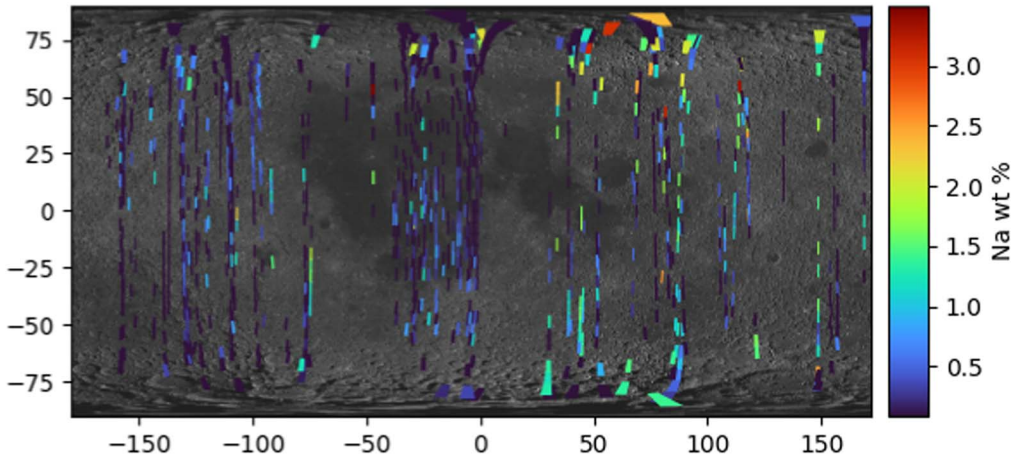

Figure 6. Sodium abundance in weight% overlaid on a LROC WAC global albedo map. Abundance increases toward higher latitudes for a given longitude.

flux consists of (i) a single component from lunar regolith and (ii) two components with a fraction of the XRF signal coming from a surface adsorbate layer (Figure 7). The Na/Mg XRF line flux ratio would vary differently with an increase in Na wt% in both cases, as shown in Figures 7(a) and (b). A two-component model provides a superior fit to the data (global

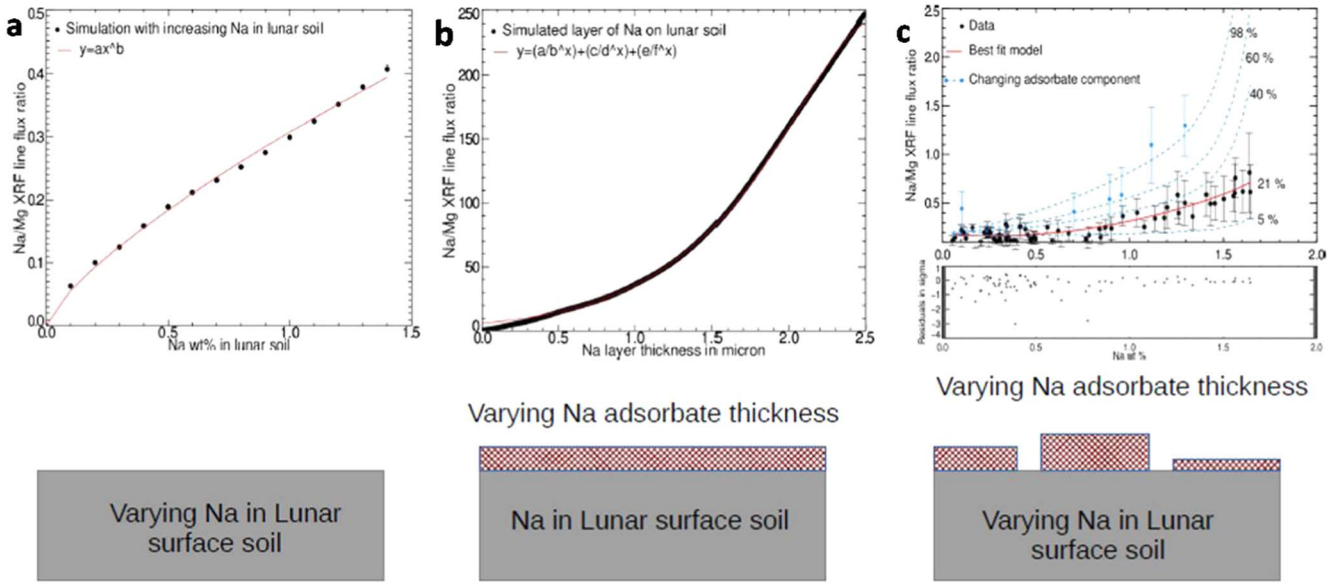

Figure 7. A two-component model (c) that consists of a regolith component and a surface adsorbate is fitted to the Na wt% data. The plot shows the variation of the Na/Mg XRF line flux ratio (a) with Na wt%, if the Na was only in the soil, and (b) with an adsorbate layer thickness if there is a component from a surface adsorbate layer as well. The red line in (c) is the best fit which gives an adsorbate component of 21%. The blue data points in (c) are not included in the fit and follow a trend of a higher fraction of adsorbate component.

data with an uncertainty lower than 25% of the value) shown in Figure 7(c). The best-fit model suggests that 21% of the observed signal is attributed to an adsorbed sodium component on average. Models for higher adsorbate components are also shown in the figure with data points that follow the corresponding trends. With the simulations as reference, the adsorbate layer should not exceed 0.05 μm in thickness.

3.2. Dependence on the Local Solar Time

Adsorbed atoms are generally weakly bound to the surface and can be released when sufficient energy is provided. Whichever is the process of release (e.g., thermal desorption or photodesorption), the adsorbate content is likely to vary with time. We divided the data sets based on the LST at the time of observation and took a weighted average across latitudes. As shown in Figure 8, sodium decreases significantly from a high value in the early morning to lower values, and tends to increase from 16:00 LST. As the number of data points at each LST is limited, we could not differentiate any trends in the LST as function of latitude. However, Na wt% shows a clear dependence on LST while Mg, an element with a similar mass as sodium that can be used as a control case, shows (1) a clear geochemical trend (Mg abundances broadly anticorrelate with the Al abundances, as expected, since the host minerals are different), with measurements over mare and the South Pole–Aitken basin having high values (Figure 9), (2) no particular enhancement at high latitudes, and (3) no diurnal effect (Figure 10).

3.3. Geochemical Component

The depletion of moderately volatile elements in the bulk Moon results from the Earth–Moon formation processes and its subsequent evolution. There are several model scenarios that could lead to an average depletion of four times compared to Earth's mantle observed (Kato et al. 2015; Canup et al. 2015; Steenstra et al. 2018; Nie & Dauphas 2019; Righter 2019) in the lunar samples. There is, however, a wide range in sodium

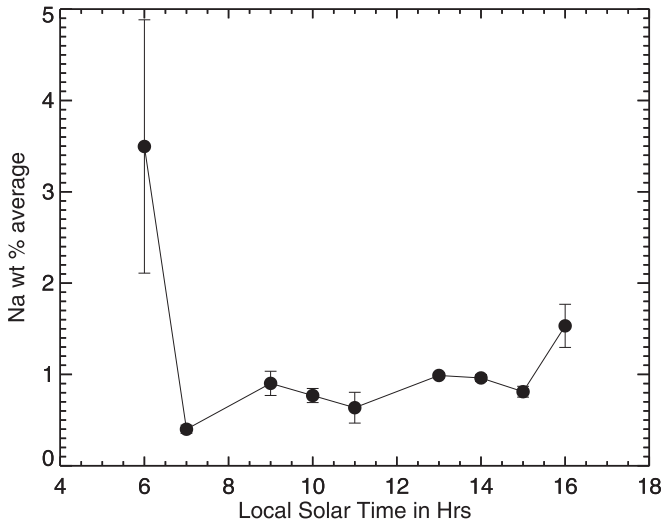

Figure 8. Variation in Na wt% as a function of LST. A significant decrease in Na wt% is measured at 07:00 LST followed by a sinusoidal trend which again tends to increase at 16:00 LST.

values even in the spatially limited lunar samples, which may require specific post formation processes and conditions. Sodium does not correlate with any of the major elements in the returned samples indicating its presence in more than one lunar mineral. Among the returned soil samples Apollo 120543 and Chang'e-5 (Tian et al. 2021) have the highest values of 0.645 wt% and 0.72 wt%, respectively. Brecciated lunar meteorites on an average have sodium abundances of 0.23 wt% except for the regolith portion of the composite lunar meteorite Sayh al Uhaymir (SaU) 169 (Al-Kathiri et al. 2007) at 1.13 wt%. The sodium abundances determined here are plotted in Figure 11. Assuming negligible adsorbate in pixels of low sodium abundances, the plot follows the general trend in the returned samples. Clearly, there is a wider range in the sodium abundances and, as in the samples, sodium does not have a simple mare–highland bimodal distribution (Figure 12). The

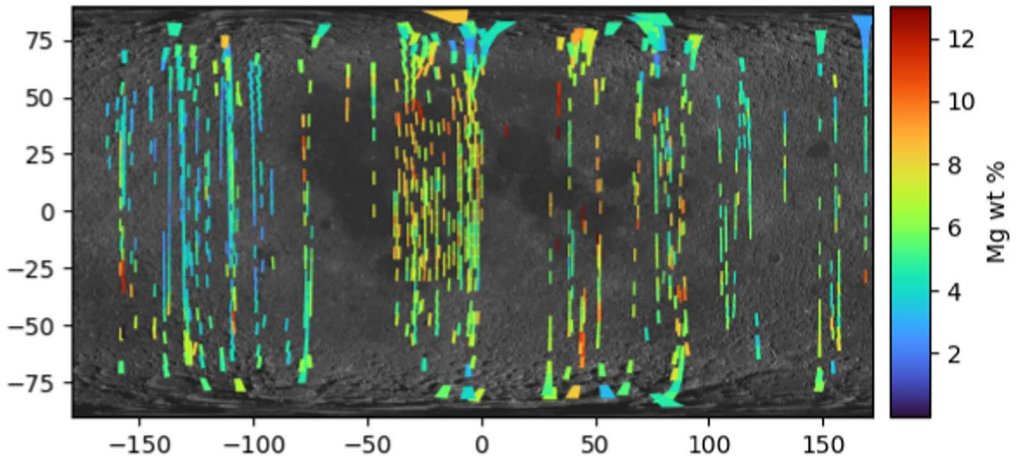

Figure 9. Mg abundance map (150 km × 12.5 km) showing the known lunar geochemical trend.

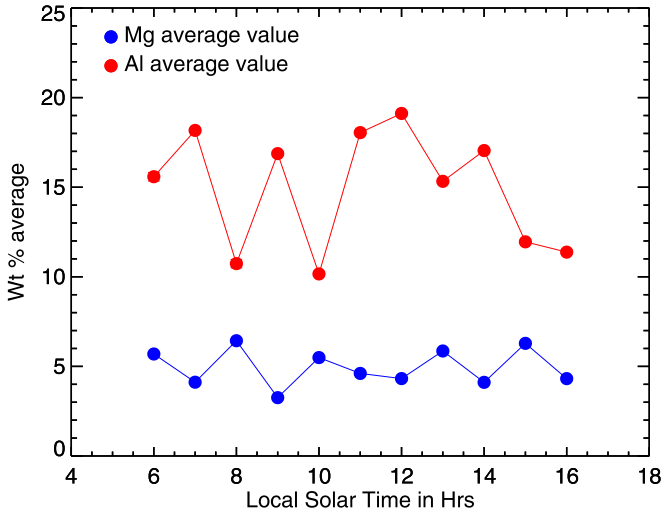

Figure 10. Mg and Al abundance averaged across latitudes do not show a trend for Na vs. LST. Mg and Al anticorrelate, as expected, for the lunar surface.

global average over all longitudes shows that overall the abundances are higher toward the northern hemisphere (Figure 13).

A similar asymmetry for the Na surface measurements is inferred on Mercury as well, attributed to the presence of alkali feldspars (Peplowski et al. 2014; Merkel et al. 2018). Recently, Czajka et al. (2022) used Lyman-Alpha Mapping Project (LAMP) Off (170–185 nm) and On (148–164 nm) band ratio maps to suggest feldspathic lithologies, including alkaline feldspar, at Aristarchus crater. However, current scenarios of the lunar crustal evolution support calcic plagioclase feldspars as the dominant component. Lunar water abundances also exhibit a north–south asymmetry (Suzuki et al. 2021) in which case the asymmetry observed here could be related to the ability of the lunar surface regolith to retain volatiles. Further investigation on the possible reversal of the asymmetry in abundance at the lunar poles over a year will be possible with more data points.

4. Discussion

Global-scale measurements of the sodium on the lunar surface presented here show that the average abundance is 1.33 ± 0.03 wt%, which is almost double of those measured in the returned samples. We propose that the sodium distribution in the upper layers of the regolith has an adsorbate component in addition to the geochemical fraction in the regolith. A good fraction of the atoms released by sputtering and meteoritic impacts could return to the surface. Alkali atoms form weak bonds when deposited on metal and metal-oxide surfaces, the nature of which is an active area of research owing to diverse applications (Riffe et al. 1990; Raghavan et al. 2021). These bonds can be overcome at high surface temperatures or under UV photon bombardment, and atoms return to the exosphere. X-ray measurements appear to be sensitive to this thin veneer of atoms that cover lunar grains and measure its variation over a lunar day. The only in-orbit exospheric measurements of the lunar sodium were obtained from LADEE over a narrow range of mid-latitudes ($\sim -21^\circ$ to $\sim -17^\circ$), in which enhancements were obtained over mare regions, intervals that also coincide with passages through the geotail (Colaprete et al. 2016). Coronographic observations of the exosphere sampled the latitudinal sodium emission at different local times and selenographic locations, showing mid-latitude enhancements (Killen et al. 2019, 2021) as well as asymmetries in the exospheric column density profiles. The surface sodium measurements are roughly consistent with the exospheric profile, suggesting a direct connection between the surface and exosphere. Sarantos & Tsavachidis (2020) simulated the effects of the microphysical properties of the regolith on the release rates of alkali adsorbates on the Moon. Two end-member models for neutral Na atoms in the exosphere, and by extension adsorbates trapped on the surface, were suggested. Sodium gas atoms observed at any moment could have been either recently released (less than a lunar day) or liberated from grains long ago (several lunar days), depending on whether the surface properties help adsorbates dislodge from microshadows (e.g., surface diffusion). If the changes of surficial sodium with local time and latitude observed here are attributable to adsorbates, as we suggest, these findings appear to support the latter of these end-member models because the adsorbate coverage would have a more pronounced variation with local time in that model, increasing in the afternoon, during night, and through sunrise, and depleted by gas desorption near local noon. Over time more sodium is lost from the Moon via losses to space in this model because in the former model the lifetime of adsorbates is limited only by the gardening rate.

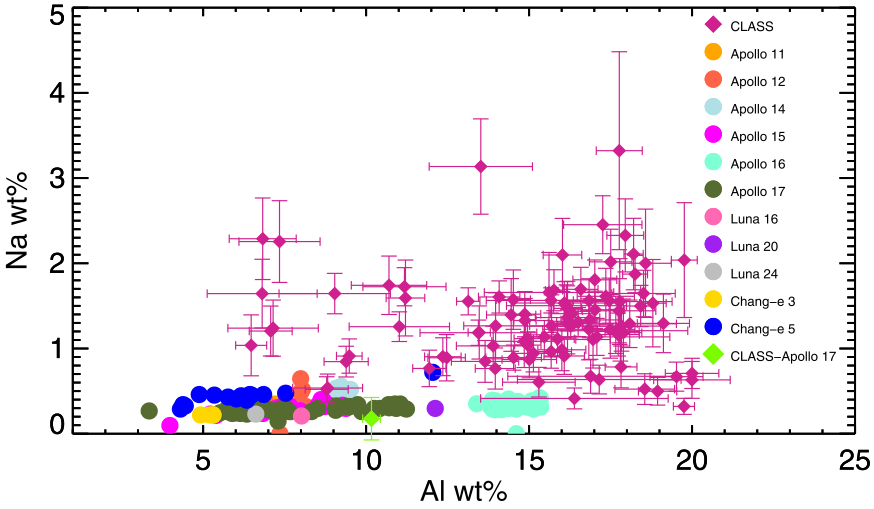

Figure 11. Variation of Na with Al does not show any correlation similar to the trend in the returned soil samples. The CLASS pixel containing the Apollo-17 landing site is marked separately.

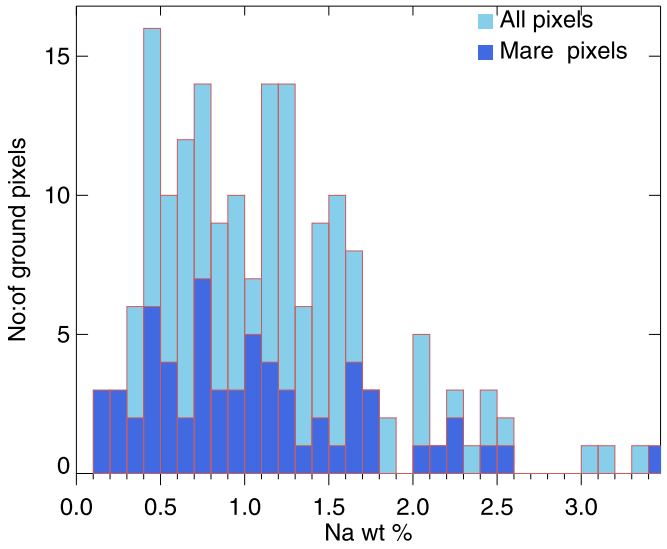

Figure 12. A histogram of the Na wt% is shown here. Ground pixels intersecting mare are colored in dark blue. There is no trend that suggests a different distribution in mare regions.

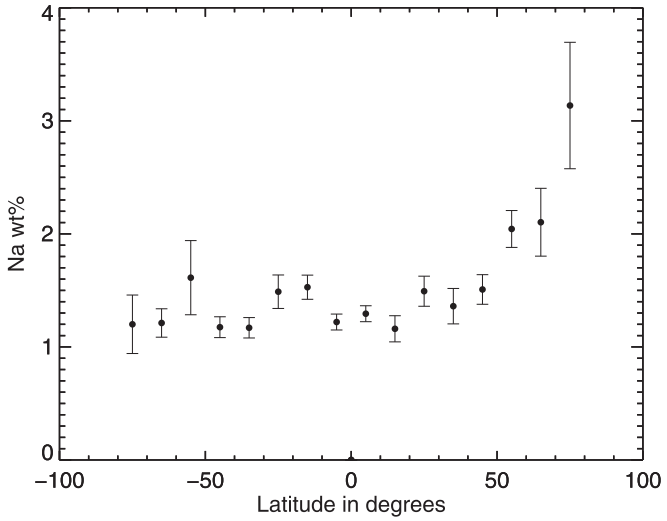

Figure 13. The global average of the latitudinal trend shows a north–south asymmetry.

5. Summary and Conclusions

In summary, the sodium distribution on the lunar surface has been mapped for the very first time. While the range of sodium wt% in lunar samples is a subset of the measurements here, on average we find higher sodium abundances. We show that the abundance distribution is best explained as arising from two components on the lunar surface that contribute to the XRF signal. We attribute the higher abundances measured to this additional component arising from an adsorbed layer of sodium. The diurnal variation and latitudinal dependence on the sodium distribution provides evidence for an active cycle that prevails on the Moon and other bodies with a surface boundary exosphere. The findings are central to models of such systems not just in our solar system but in exoplanetary systems too. With the solar cycle in its ascent, CLASS will provide global maps of Na in the coming years.

We are grateful to P. Sreekumar, Satish Dhawan Professor ISRO HQ, Megha Bhatt, Physical Research Laboratory (PRL), and A. S. Kiran Kumar, Vikram Sarabhai Professor, ISRO HQ for active discussions on the results presented here. We acknowledge the support from M. Vanitha, Project Director, Chandrayaan-2, Ritu Karidhal, Mission Director, Vaishali Sharan, CLASS data pipeline and archival, URSC and the spacecraft data processing team at ISSDC, ISRO.

ORCID iDs

S. Narendranath https://orcid.org/0000-0001-9199-4925
Menelaos Sarantos https://orcid.org/0000-0003-0728-2971

References

Agostinelli, S., Allison, J., Amako, K., et al. 2003, NIMPA, 506, 250
Al-Kathiri, A., Gnos, E., & Hofmann, B. A. 2007, M&PS, 42, 2137
Athiray, P. S., Narendranath, S., Sreekumar, P., Dash, S. K., & Babu, B. R. S. 2013a, P&SS, 75, 188
Athiray, P. S., Narendranath, S., Sreekumar, P., & Grande, M. 2014, P&SS, 104, 279
Athiray, P. S., Sreekumar, P., Narendranath, S., & Gow, J. P. D. 2015, A&A, 583, A97
Athiray, P. S., Sudhakar, M., Tiwari, M. K., et al. 2013b, P&SS, 89, 183
Baumgardner, J., Luettgen, S., Schmidt, C., et al. 2021, JGRE, 126, e06671

Canup, R. M., Visscher, C., & Fegley, B. J. 2015, NatGe, 8, 918
Colaprete, A., Sarantos, M., Wooden, D. H., et al. 2016, Sci, 351, 249
Czajka, E. A., Retherford, K. D., Kramer, G., et al. 2022, LPICo, 53, 2162
Grande, M., Kellett, B., Howe, C., et al. 2007, P&SS, 55, 494
Grande, M., Maddison, B. J., Howe, C. J., et al. 2009, P&SS, 57, 717
Kato, C., Moynier, F., Valdes, M. C., Dhaliwal, J. K., & Day, J. M. D. 2015, NatCo, 6, 7617
Katsuda, S., Ohno, M., Mori, K., et al. 2020, ApJ, 891, 126
Keller, L. P., & McKay, D. S. 1993, Sci, 261, 1305
Killen, R. M., Morgan, T. H., Potter, A. E., et al. 2019, Icar, 328, 152
Killen, R. M., Morgan, T. H., Potter, A. E., et al. 2021, Icar, 355, 114155
Lodders, K. 2003, APJ, 591, 1220
Lowe, B., Holland, A., Hutchinson, I., Burt, D., & Pool, P. 2001, NIMPA, 458, 568
Merkel, A. W., Vervack, R. J., Killen, R. M., et al. 2018, GeoRL, 45, 6790
Merkel, A. W., Vervack, R. J., Jr+, Killen, R. M., et al. 2018, GeoRL, 45, 6790
Mithun, N. P. S., Vadawale, S. V., Sarkar, A., et al. 2020, SoPh, 295, 139
Mondal, B., Sarkar, A., Vadawale, S. V., et al. 2021, ApJ, 920, 4
Narendranath, S., Athiray, P. S., Sreekumar, P., et al. 2011, Icar, 214, 53
Narendranath, S., Sreekumar, P., Pillai, N. S., et al. 2020, SoPh, 295, 175
Nie, N. X., & Dauphas, N. 2019, ApJL, 884, L48
Peplowski, P. N., Evans, L. G., Stockstill-Cahill, K. R., et al. 2014, Icar, 228, 86
Pillai, N. S., Narendranath, S., Vadodariya, K., et al. 2021, Icar, 363, 114436
Potter, A. E., & Morgan, T. H. 1988, Sci, 241, 675
Raghavan, A., Slocombe, L., Spreinat, A., et al. 2021, PCCP, 23, 7822
Riffe, D. M., Wertheim, G. K., & Citrin, P. H. 1990, PhRvL, 64, 571
Righter, K. 2019, SciA, 5, eaau7658
Ringwood, A. E., & Kesson, S. E. 1977, Moon, 16, 425
Sarantos, M., & Tsavachidis, S. 2020, GeoRL, 47, e88930
Shiraiwa, T., & Fujino, N. 1966, JaJAP, 5, 886
Smith, P., Gow, J., Murray, N., et al. 2014, JInst, 9, P04019
Smith, S. M., Wilson, J. K., Baumgardner, J., & Mendillo, M. 1999, GRL, 26, 1649
Steenstra, E. S., Agmon, N., Berndt, J., et al. 2018, NatSR, 8, 7053
Suzuki, Y., Yoshioka, K., Murakami, G., & Yoshikawa, I. 2021, Earth and Space Science Open Archive 18, doi:10.1002/essoar.10507933.1
Szalay, J. R., Horányi, M., Colaprete, A., & Sarantos, M. 2016, GeoRL, 43, 6096
Tian, H.-C., Wang, H., Chen, Y., et al. 2021, Natur, 600, 59
Vatedka, R., Tyagi, A., Narendranath, S., et al. 2020, CSci, 118, 219
Weider, S. Z., Kellett, B. J., Swinyard, B. M., et al. 2012, P&SS, 60, 217
Wood, B. J., Smythe, D. J., & Harrison, T. 2019, AmMin, 104, 844
Yamashita, N., & Prettyman, T. H. 2021, LPI, 52, 1633
Zhang, S.-N., Li, T., Lu, F., et al. 2020, SCPMA, 63, 249502